THE JOURNAL OF
PHYSICAL CHEMISTRY
LETTERS
A JOURNAL OF THE AMERICAN CHEMICAL SOCIETY

pubs.acs.org/JPCL
Letter

Memristive Response and Capacitive Spiking in Aqueous Ion Transport through Two-Dimensional Nanopore Arrays

Yechan Noh and Alex Smolyanitsky*

Cite This: *J. Phys. Chem. Lett.* 2024, 15, 665−670

Read Online

ACCESS | Metrics & More | Article Recommendations | SI Supporting Information

ABSTRACT: In living organisms, information is processed in interconnected symphonies of ionic currents spiking through protein ion channels. As a result of dynamic switching of their conductive states, ion channels exhibit a variety of current−voltage nonlinearities and memory effects. Fueled by the promise of computing architectures entirely different from von Neumann, recent attempts to identify and harness similar phenomena in artificial nanofluidic environments focused on demonstrating analogue circuit elements with memory. Here we explore aqueous ionic transport through two-dimensional (2D) membranes featuring arrays of ion-trapping crown-ether-like pores. We demonstrate that for aqueous salts featuring ions with different ion−pore binding affinities, memristive effects emerge through coupling between the time-delayed state of the system and its transport properties. We also demonstrate a nanopore array that behaves as a capacitor with a strain-tunable built-in barrier, yielding behaviors ranging from current spiking to an ohmic response. By focusing on the illustrative underlying mechanisms, we demonstrate that realistically observable memory effects may be achieved in nanofluidic systems featuring crown-porous 2D membranes.

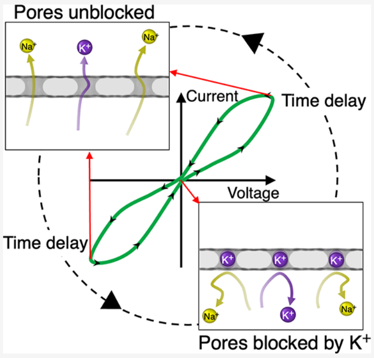

Although the first memory-enabled resistor, or memristor, was formally proposed in 1971,[1] similar devices have been considered as interconnected building blocks in artificial neural networks since at least the 1960s.[2] The search for practical neuromorphic computing implementations has now evolved into a vast multidisciplinary field that ranges from materials science[2−8] and physics of dynamic systems[2,5,6,8] to information processing algorithms.[7,9] In the past five years, numerous nanofluidic devices featuring memory effects in their current−voltage response have been reported.[10−16] The memory effects have been shown to arise from local time delays introduced by ion concentration polarization caused by high electric fields,[10] diffusivity-limited dynamics,[11,12,16] the Wien effect,[14,15] and adsorption−desorption processes in confined electrolytes.[14,16] These mechanisms are of little surprise, resulting from the fundamental ubiquity of local time delays built into the dynamic response of essentially any realistic system, as predicted by the Kubo response theory[17] and conceptually detailed by Di Ventra and Pershin specifically for memory-featuring versions of basic circuit elements such as resistors, capacitors, and inductors.[18] In the context of nanofluidic systems, time delays arising from mechanisms that can be broadly classified as diffusion-limited and adsorption−desorption processes are required to build a realistic circuit element featuring memory. At the same time, in systems involving water as the only solvent, remembered states tend to dissipate rapidly, often within picoseconds. Therefore, reducing the memory volatility is a fundamental challenge for harnessing memory effects in aqueous environments. Toward this goal, a clear understanding of the mechanisms that yield distinct and measurable memory effects in nanofluidic systems is critical.

In this work, we use all-atom molecular dynamics (MD) simulations to describe highly illustrative memory and spiking phenomena in dynamically biased nanofluidic systems that do not rely on high-viscosity solvents, conical pore geometries, or the two-dimensional (2D) confinement of aqueous electrolytes. We first describe memristive transport through arrays of graphene-embedded crown pores in the presence of aqueous salt mixtures and explain how the dynamic sieving of two salts, neither of which individually yields memory effects, can be a memristor through a straightforward coupling between the state of the system and its transport properties. In addition, we demonstrate ion current spiking dynamics in the case of a hexagonal boron nitride (hBN) monolayer featuring an array of triangular nitrogen-terminated crown-like pores. Such a system is shown to be essentially a capacitive element with a built-in chemical barrier. We finally demonstrate that this barrier can be modulated by a tensile strain applied to the membrane, causing a transition in the dynamic transport response from spiking to the tell-tale behavior of an RC circuit.

Received: November 9, 2023
Revised: January 4, 2024
Accepted: January 5, 2024
Published: January 11, 2024

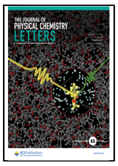

https://doi.org/10.1021/acs.jpclett.3c03156

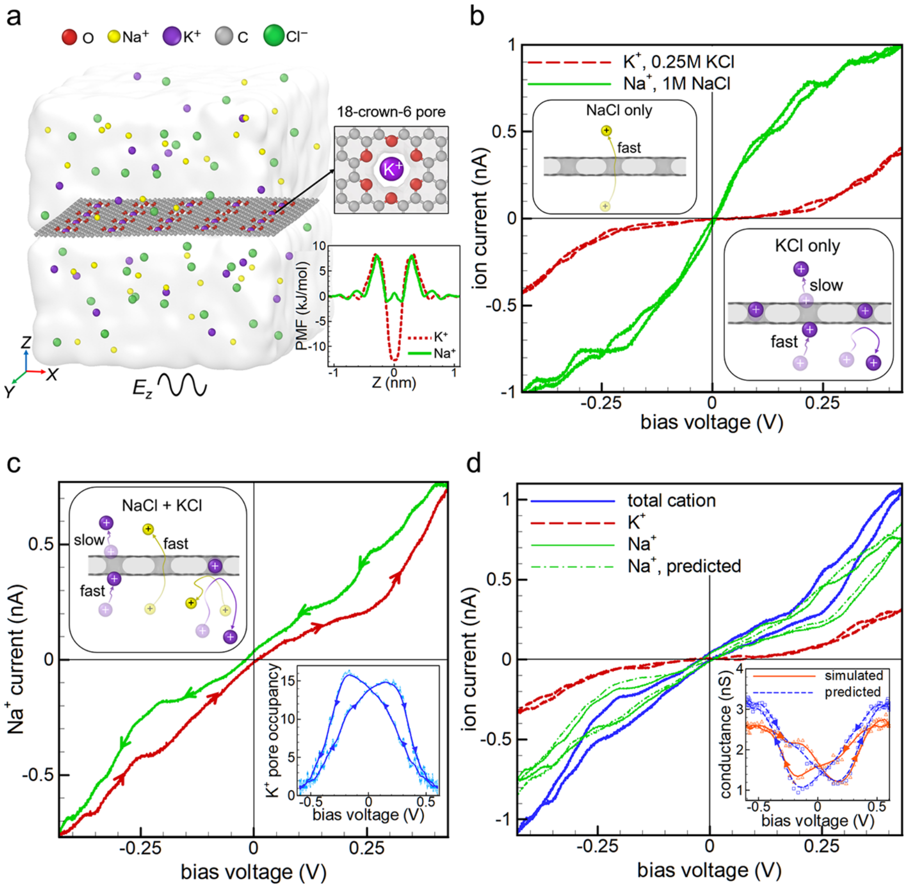

Figure 1. Dynamic current−voltage response of aqueous crown-porous graphene. (a) Simulated system with the PMF curves for Na^+ and K^+ ions, (b) Lissajous curves for Na^+ and K^+ currents in individual salt simulations of 1 M NaCl and 0.25 M KCl, respectively, (c) Lissajous curve for the Na^+ current obtained from a 1 M NaCl/ 0.25 M KCl mixture, and (d) simulated Na^+ current compared with the prediction based on the pore occupancy by the K^+ ions, along with the total (K^+ and Na^+) cation current. The Lissajous curve for the K^+ pore occupancy is shown in the bottom right part of panel c. The inset of panel d shows the Lissajous curve for the total simulated system conductance compared with the analytical estimate based on the occupancy, as described in the text. The continuous curves for simulated and predicted data are visual guides obtained from smoothing the corresponding raw data points (triangles and squares, respectively). All figures correspond to a bias field oscillation frequency of 5 MHz. Given the high density of the ionic current data presented here, the corresponding uncertainty bars have been omitted for the sake of clarity. The average numerical uncertainties for the Na^+ and K^+ currents reported in this figure are 0.098 and 0.052 nA, respectively.

Our first example is a locally suspended graphene monolayer featuring a 4 × 5 array of 18-crown-6 pores,[19−22] immersed in an aqueous salt bath and subject to a sinusoidal external bias along the Z-direction, as sketched in Figure 1a. The simulation details are provided in Methods. A key property of these subnanometer pores is that they selectively trap aqueous K^+ cations, in contrast with Na^+, which permeate rapidly without being trapped. As discussed in detail previously,[20,21] this property of crown pores is in accord with the selective binding between 18-crown-6 molecules and alkali cations,[23] a hallmark example of selective affinity in the field of coordination chemistry. The corresponding Gibbs free energy distributions in the form of potential of mean force (PMF) curves are shown in Figure 1a, indicating that in the absence of external bias, K^+ ions encounter a significant potential well at the center of the pore, while the Na^+ ions do not. As discussed below, this selective affinity will prove central to the mechanism underlying memory phenomena in this case.

Consider Figure 1b, which shows the K^+ and Na^+ currents obtained from single-salt simulations of 0.25 M KCl and 1 M NaCl, respectively. The currents are plotted as Lissajous curves, i.e., direct functions of the sinusoidal bias voltage $V(t) = V_0 \cos(\omega t)$, where in this case $V_0 = hE_0 = 0.6$ V ($h \approx 6$ nm, and $E_0 = 0.1$ V/nm) and $\omega/2\pi = 5$ MHz. As shown, neither curve exhibits appreciable hysteretic behavior. Let us now combine these salts, at the same individual concentrations, into a binary mixture (0.25 M KCl/1 M NaCl) and consider the resulting Na^+ current shown in Figure 1c. Hysteresis is now observed between the ion current branches corresponding to the rising and falling edges of the sinusoidal bias, indicative of broadly memristive transport. To understand why the transport of a mixture of two salts, neither of which individually yields ion current hysteresis, exhibits memristive behavior, we must realize that crown pores conduct one ion at a time in a mutually exclusive manner. In single-salt scenarios, the cations in question permeate, as sketched in the insets of Figure 1b. K^+ ions are trapped by the pores, causing them to permeate slowly one ion at a time; in contrast, Na^+ ions permeate rapidly without trapping, while anions (not shown) are outright rejected due to incompatible dipole electrostatics at the pore interior.[20] As demonstrated previously for binary mixtures,[21] transport occurs as a mostly unidirectional competition between Na^+ and K^+ ions. Recall that crown pores have a high selective affinity for K^+ ions. Therefore, Na^+ cations are statistically expected to permeate through pores unoccupied by the trapped K^+ ions, as sketched in the top left

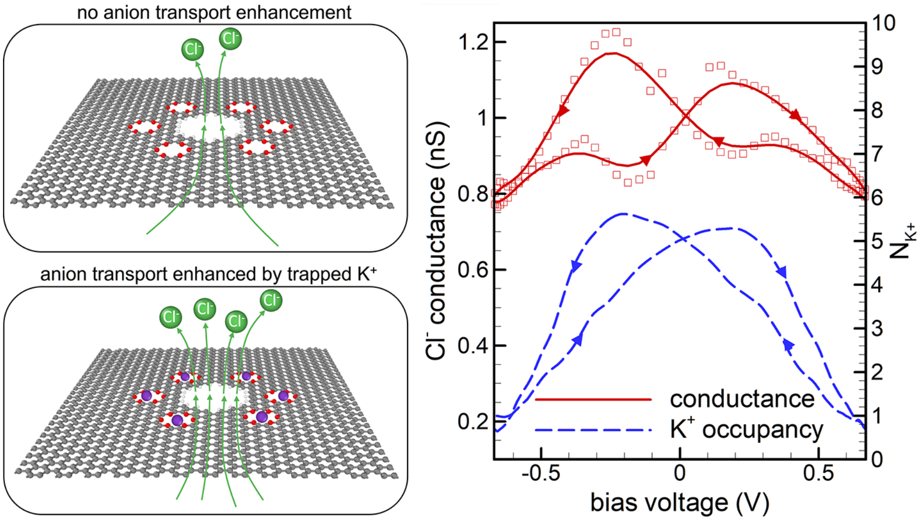

Figure 2. Anion transport enhanced by trapped K$^+$. The distinct anion transport states for the simulated porous membrane are shown on the left. Anion conductance $G_{\mathrm{Cl}^-}(t) = I_{\mathrm{Cl}^-}(t)/V(t)$ and K$^+$ occupancy are plotted on the right. The continuous Lissajous curve for $G_{\mathrm{Cl}^-}(t)$ is a visual guide obtained from smoothing the corresponding raw data points (squares). The data on the right were simulated in a box for which h = 9 nm and E_0 = 0.075 V/nm at $\omega/2\pi$ = 5 MHz. The estimated bias voltage amplitude $V_0 = hE_0$ = 0.675 V. The average numerical uncertainty for the Cl$^-$ ionic currents underlying the data in this figure is 0.045 nA.

inset of Figure 1c. In contrast, K$^+$ transport is not hampered by the presence of Na$^+$, because the latter permeates rapidly without being trapped. A reasonably detailed treatment based on the modified Langmuir model[24] is possible for this competition, as presented in the supplementary section S3 of our earlier work.[21] For the purpose of this discussion, a more tacit argument is provided. Depending on the bias, the number of pores clogged by the trapped K$^+$ ions is a dynamic function that naturally carries delay from the finite times it takes the K$^+$ ions to cumulatively occupy or leave the pores, as shown for sinusoidal bias in the bottom right inset of Figure 1c. Given that the time taken by the K$^+$ ions to populate the pore array is mainly determined by a diffusive process,[25] the corresponding time delay associated with the memristive response is expected to be able to be tuned by the K$^+$ concentration. The latter could be adjusted to achieve a memristive response at bias frequencies considerably lower than those considered here. It should then be clear that we selected a relatively low KCl concentration of 0.25 M (compared with 1 M NaCl) to achieve an observable delay and to reduce the K$^+$ contribution to the overall cation transport, all while maintaining robust data collection within microseconds of total simulated time. If the ion–ion knock-on phenomena are neglected, the pore occupancy by the pore-clogging K$^+$ ions is thus the system state that governs Na$^+$ transport in a mixture. Let us denote the occupancy $N_{\mathrm{K}^+}(t)$ and point out a few noteworthy aspects. First, K$^+$ permeation, as both a single salt or in a mixture involving Na$^+$, does not depend on $N_{\mathrm{K}^+}(t)$,[21] because the charge carriers and the pore-blocking ions are identical and thus essentially all pores are available for K$^+$ permeation. This is consistent with nearly the same nonhysteretic K$^+$ current data in panels b and d of Figure 1. Second, $N_{\mathrm{K}^+}(t)$ is likely to be directly observable in the form of electrical potential measured at the membrane, as described previously for dc bias.[20] This measurement of the electrical potential is expected to be significantly less affected by the bandwidth limitations associated with, for example, ion current measurements. Finally, $N_{\mathrm{K}^+}(t)$ can be used as an elementary coupling term to predict the Na$^+$ current for the NaCl/KCl mixture. If the total number of pores in the system (N_0) is 20, only those unoccupied by K$^+$ are available for Na$^+$ transport. The Na$^+$ current for a mixture is then estimated as $I^{\mathrm{mix}}_{\mathrm{Na}^+}(t) = I_{\mathrm{Na}^+}(t)\left[1 - \frac{N_{\mathrm{K}^+}(t)}{N_0}\right]$, where $I_{\mathrm{Na}^+}(t)$ is the nonhysteretic single-salt Na$^+$ current response from Figure 1b. The comparison between this estimate and that simulated in an actual mixture (data also shown in Figure 1c) is shown in Figure 1d. An overall reasonable agreement between the two Lissajous curves suggests that the observed dynamic mixture sieving is an example of a system in which the current–voltage response is an illustratively simple linear function of the system state. For further qualitative comparison, see the inset of Figure 1d, where the total conductance $G(t) = I(t)/V(t)$ (including both K$^+$ and Na$^+$ contributions) simulated in the mixture is compared with the analytical estimate given by $I^{\mathrm{tot}}(t) = I^{\mathrm{mix}}_{\mathrm{Na}^+}(t) + I_{\mathrm{K}^+}(t)$, where $I^{\mathrm{mix}}_{\mathrm{Na}^+}(t)$ is as defined above and $I_{\mathrm{K}^+}(t)$ is the nonhysteretic K$^+$ contribution from the single-salt data in Figure 1b. Both curves are shown to qualitatively inherit the time dependence of K$^+$ occupancy as a function of time (see the bottom right inset of Figure 1c).

The state-transport coupling through direct blockage of conductive paths by trapped ions is one example. A less direct coupling is demonstrated in Figure 2, where the system is similar to that described above, except the graphene membrane features a relatively wide ($d \approx 1.5$ nm) pore, closely surrounded by six crown-like pores. Here, K$^+$ trapping results in a ring of temporarily immobile charge, which at sufficiently low ion concentrations is expected to modulate anion transport[26−28] by attracting counterions (Cl$^-$) toward the large pore. This field-induced coupling can be directly observed here because anions have no affinity for the crown pores, permeating only through the wide pore. No cation mixture is required in this case, and we use KCl at a concentration such that the corresponding Debye screening length is comparable to the radius of the wide pore (0.15 M). Although less pronounced than in the case presented above, memristive anion transport is indeed revealed in the right panel

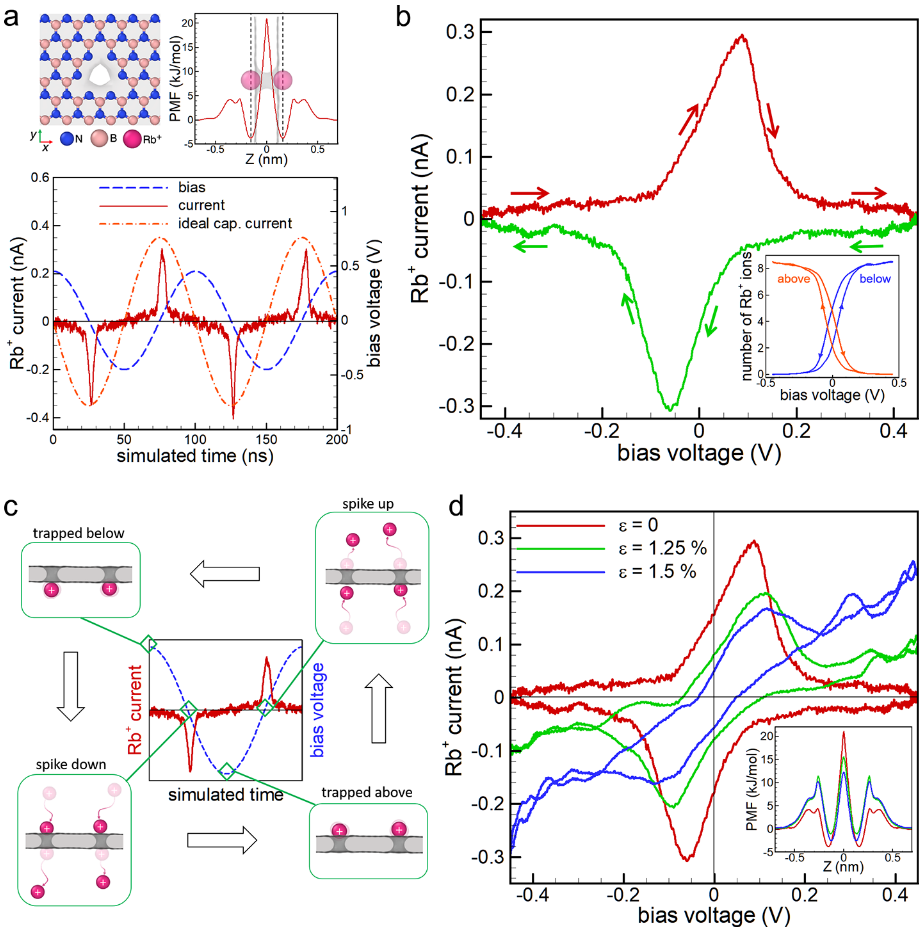

Figure 3. Spiking capacitive Rb^+ currents through subnanometer-porous hBN. (a) Pore structure, the corresponding PMF curve for Rb^+ ions, and the simulated ionic current as a function of simulated time and (b) the corresponding Lissajous curve; (c) a sketch of the system state dynamics; and (d) Lissajous curves for Rb^+ currents through pores with the corresponding PMF curves shown in the inset. The inset in panel b shows the Lissajous curves of the ion occupancy above and below the membrane's geometric midline. All figures correspond to a bias field oscillation frequency of 10 MHz. The average numerical uncertainty for the ionic currents reported in this figure is 0.025 nA.

of Figure 2, similar to that in the inset of Figure 1d, except here the hysteretic accumulation of trapped K^+ enhances the transport of another ionic species instead of hampering it.

Our second example is similar to those presented above, except the membrane is monolayer hBN featuring a 3 × 3 array of nitrogen-terminated triangular pores, one of which is shown at the top of Figure 3a. For these subnanometer pores, the dipolar pore edge with partial negative charges carried by the nitrogen atoms at the perimeter[29] generally yields crown-like properties, which include cation trapping and broad anion rejection, thus making the phenomena described above generally expected here, as well. On this occasion, however, we explore a pore impermeable to a selected ionic species, resulting in a qualitatively different scenario. We chose 1 M RbCl, and the corresponding PMF curve for the Rb^+ ion is provided in Figure 3a. In addition to being impermeable due to a large peak at the pore's geometric midline, the pore features two relatively weak binding sites ≈0.16 nm above and below the midline. Note that ion−ion Coulomb repulsion causes the two bound states to be mutually exclusive; i.e., only one ion at a time can bind on either side.

The Rb^+ current as a function of time in response to a sinusoidal bias with a V_0 of 0.45 V and an $\omega/2\pi$ of 10 MHz is shown at the bottom of Figure 3a, alongside $V(t)$ and the ideal capacitive current $\left(\propto \frac{\mathrm{d}V}{\mathrm{d}t}\right)$ provided as references. In contrast with the gradual discharge of an ideal capacitor, we see bidirectional ≈15 ns-wide current spikes near $V = 0$ crossings, all attributed to the rapid release of ions, depending on the bias polarity in relation to the current charging state. The corresponding Lissajous curve is shown in Figure 3b. The spiking dynamics here is due to the presence of a chemical barrier built into this capacitor, and a simple "state diagram" in Figure 3c is provided to describe the switching cycle and explain the presence of elementary directional memory. Overall, this system can be viewed as a simple spiking NOT-gate with polarity awareness. Zero bias voltage (input) results in a current (output) upspike if the previous input was negative and vice versa. We note that the charge/discharge curves (in the form of pore occupancies) "above" and "below" shown in the inset of Figure 3b are indicative of an accompanying memcapacitive effect, resulting from time delays caused by mechanisms similar to those discussed above. The "firing" dynamics of the ionic currents should be tunable in terms of the peak height and width/phase, as determined by the total pore count and the barrier shape, respectively. We also note that weakened binding (while maintaining pore impermeability) would bring the peaks of the two Lissajous branches in Figure 3b closer to zero voltage and also widen them toward

https://doi.org/10.1021/acs.jpclett.3c03156
J. Phys. Chem. Lett. 2024, 15, 665−670

semicircles, essentially approaching the dynamic response of an ideal capacitor. While testing these behaviors would be beyond the scope of this work, here we can briefly explore a change in transport response as we tune the ion−pore interactions by applying isotropic strain to the hBN membrane. The Lissajous curves for the Rb^+ currents, along with the corresponding PMF data, are shown in Figure 3d. It is clear that upon application of membrane strain and dilation of the pores, the central barrier is reduced, causing ion permeation and thus a transition from capacitive to RC circuit behavior, which at even higher strains we expect to approach the ohmic response. Once again, the simplicity here is illustrative, suggesting nanofluidic "gates" with dynamic transport response tuned by strain or an auxiliary electrostatic bias, possibly dynamically.

To summarize, we have demonstrated memristive effects and spiking behavior of dynamically biased aqueous ion transport through 2D materials featuring arrays of crown-like subnanometer pores. The mechanisms are shown to include competitive sieving of ion mixtures, resulting in a coupling between the time-delayed state of the system and its transport properties, as well as capacitive charging and discharging in the presence of built-in chemical barriers. The phenomena described above are highly illustrative and suggest that nanofluidic systems based on subnanoporous 2D materials may be an intriguing choice for achieving analog−digital hybrids that can be used in artificial neural networks, especially if aimed at dynamics in the range from tens to hundreds of kilohertz to megahertz. By focusing on the mechanisms rather than specific applications, we hope to elucidate the physics of realistically observable dynamic effects in nanofluidic ion transport and further stimulate experimental efforts. First and foremost, this includes the fabrication of predictable, chemically stable pore structures with various degrees of affinity for aqueous solutes.

■ METHODS

All MD simulations were performed using GPU-accelerated GROMACS version 2023.2 within the OPLS-AA[30] framework. Each simulation of ion transport was carried out in a nearly cubic box with a side of ≈6 nm, periodic in *XYZ*, and containing a porous monolayer of graphene or hBN, TIP4P[31] water, and dissociated salts at concentrations stated in the text. The membranes were kept in place by harmonic restraints applied at the perimeter. Previously established models for crown-porous graphene[20,21] and hBN[32] were used within the OPLS-AA force field. The partial charges of nitrogen atoms lining the triangular pore edges in hBN were set to 2/3 of those for bulk nitrogen atoms, ensuring charge neutrality of the pore structures. Electrostatic interactions were resolved using the particle−particle—particle−mesh scheme with short-range interaction cutoff radii of 1.0 and 1.2 nm for the simulations involving graphene and hBN, respectively. Prior to the production simulations, all systems underwent static energy minimization, 5 ns of semiisotropic (constant in-plane cell dimensions) *NPT* relaxation at 300 K and 0.1 MPa with a time step of 1 fs. Each production simulation was performed in the *NVT* ensemble with a time step of 2 fs under sinusoidal external field $E(t) = E_0 \cos(\omega t)$, preceded by a 10 ns prerelaxation at a constant field E_0 to reduce any spurious oscillations from the initial impulse ($E_{t=0} = E_0$). The simulated times were set to ensure 8−10 full periods of external field variation. For example, when $\omega/2\pi = 5$ MHz, the total simulated time was 2 μs, corresponding to ten 200 ns periods. Unless stated otherwise, E_0 was set to 0.075 V/nm, roughly corresponding to an effective maximum voltage of $E_0h = 0.45$ V ($h \approx 6$ nm is the box height in the *Z*-direction). The E_0 values were selected to ensure that the crown pores are depopulated by the K^+ ions at maximum bias.[20] All ion current data were obtained from numerical differentiation of the cumulative ionic fluxes, performed using finite differences at the 8th order of accuracy. Numerical differentiation is a noise-amplifying procedure, and therefore prior to differentiation, all flux data had to be filtered without introducing purely numerical memory artifacts, which was achieved through careful use of bidirectional filtering (see details in section S1 of the Supporting Information). The raw flux and occupancy data were output every 10 ps, corresponding to a maximum resolvable frequency of 50 GHz. Given that in this work the external bias oscillated at 5−10 MHz, low-pass cutoffs were typically set to the order of 200 MHz to provide ample bandwidth for capturing the dynamics of interest. The ion currents used for constructing the Lissajous curves were obtained from averaging among all simulated periods of external field oscillation, and the statements regarding uncertainties refer to the corresponding standard deviations. For further details of data processing used in this work, see section S1 of the Supporting Information. All PMF calculations were carried out in a manner similar to that of our previous work,[20,21,33] utilizing the weighted histogram analysis method[34] applied to a total of 60 0.05 nm spaced ionic configurations relative to the pore location along the *Z*-direction. The umbrella sampling of each configuration of the target ion was performed for 10 ns.

■ ASSOCIATED CONTENT

Supporting Information

The Supporting Information is available free of charge at https://pubs.acs.org/doi/10.1021/acs.jpclett.3c03156.

Data processing (section S1) and two additional references (PDF)

■ AUTHOR INFORMATION

Corresponding Author

Alex Smolyanitsky − *Applied Chemicals and Materials Division, National Institute of Standards and Technology, Boulder, Colorado 80305, United States;* orcid.org/0000-0002-4378-8155; Email: alex.smolyanitsky@nist.gov

Author

Yechan Noh − *Applied Chemicals and Materials Division, National Institute of Standards and Technology, Boulder, Colorado 80305, United States; Department of Materials Science and Engineering, University of California, Berkeley, Berkeley, California 94720, United States;* orcid.org/0000-0003-1688-4907

Complete contact information is available at:
https://pubs.acs.org/10.1021/acs.jpclett.3c03156

Notes

The authors declare no competing financial interest.

■ ACKNOWLEDGMENTS

This work was supported in part by National Science Foundation Grant 2110924. The authors are grateful to Frances Allen and Dana Byrne for illuminating discussions.

■ REFERENCES

(1) Chua, L. Memristor-The missing circuit element. *IEEE Trans. Circuit Theory* **1971**, *18*, 507−519.

(2) Yang, J. J.; Strukov, D. B.; Stewart, D. R. Memristive devices for computing. *Nat. Nanotechnol.* **2013**, *8*, 13−24.

(3) Wang, Z.; Rao, M.; Han, J.-W.; Zhang, J.; Lin, P.; Li, Y.; Li, C.; Song, W.; Asapu, S.; Midya, R.; et al. Capacitive neural network with neuro-transistors. *Nat. Commun.* **2018**, *9*, 3208.

(4) Wang, Z.; Wu, H.; Burr, G. W.; Hwang, C. S.; Wang, K. L.; Xia, Q.; Yang, J. J. Resistive switching materials for information processing. *Nat. Rev. Mater.* **2020**, *5*, 173−195.

(5) Kumar, S.; Wang, X.; Strachan, J. P.; Yang, Y.; Lu, W. D. Dynamical memristors for higher-complexity neuromorphic computing. *Nat. Rev. Mater.* **2022**, *7*, 575−591.

(6) Lanza, M.; Sebastian, A.; Lu, W. D.; Le Gallo, M.; Chang, M.-F.; Akinwande, D.; Puglisi, F. M.; Alshareef, H. N.; Liu, M.; Roldan, J. B. Memristive technologies for data storage, computation, encryption, and radio-frequency communication. *Science* **2022**, *376*, No. eabj9979.

(7) Christensen, D. V.; Dittmann, R.; Linares-Barranco, B.; Sebastian, A.; Le Gallo, M.; Redaelli, A.; Slesazeck, S.; Mikolajick, T.; Spiga, S.; Menzel, S.; et al. 2022 roadmap on neuromorphic computing and engineering. *Neuromorphic Comput. and Eng.* **2022**, *2* (2), No. 022501.

(8) Sangwan, V. K.; Hersam, M. C. Neuromorphic nanoelectronic materials. *Nat. Nanotechnol.* **2020**, *15*, 517−528.

(9) Jung, S.; Lee, H.; Myung, S.; Kim, H.; Yoon, S. K.; Kwon, S.-W.; Ju, Y.; Kim, M.; Yi, W.; Han, S.; et al. A crossbar array of magnetoresistive memory devices for in-memory computing. *Nature* **2022**, *601*, 211−216.

(10) Bu, Y.; Ahmed, Z.; Yobas, L. A nanofluidic memristor based on ion concentration polarization. *Analyst* **2019**, *144*, 7168−7172.

(11) Sheng, Q.; Xie, Y.; Li, J.; Wang, X.; Xue, J. Transporting an ionic-liquid/water mixture in a conical nanochannel: a nanofluidic memristor. *Chem. Commun.* **2017**, *53*, 6125−6127.

(12) Zhang, P.; Xia, M.; Zhuge, F.; Zhou, Y.; Wang, Z.; Dong, B.; Fu, Y.; Yang, K.; Li, Y.; He, Y.; et al. Nanochannel-based transport in an interfacial memristor can emulate the analog weight modulation of synapses. *Nano Lett.* **2019**, *19*, 4279−4286.

(13) Xiong, T.; Li, C.; He, X.; Xie, B.; Zong, J.; Jiang, Y.; Ma, W.; Wu, F.; Fei, J.; Yu, P.; et al. Neuromorphic functions with a polyelectrolyte-confined fluidic memristor. *Science* **2023**, *379*, 156−161.

(14) Robin, P.; Emmerich, T.; Ismail, A.; Niguès, A.; You, Y.; Nam, G.-H.; Keerthi, A.; Siria, A.; Geim, A.; Radha, B.; et al. Long-term memory and synapse-like dynamics in two-dimensional nanofluidic channels. *Science* **2023**, *379*, 161−167.

(15) Robin, P.; Kavokine, N.; Bocquet, L. Modeling of emergent memory and voltage spiking in ionic transport through angstrom-scale slits. *Science* **2021**, *373*, 687−691.

(16) Emmerich, T.; Teng, Y.; Ronceray, N.; Lopriore, E.; Chiesa, R.; Chernev, A.; Artemov, V.; Di Ventra, M.; Kis, A.; Radenovic, A. Nanofluidic logic with mechano-ionic memristive switches. *arXiv* **2023**, DOI: 10.48550/arXiv.2306.07617.

(17) Kubo, R. Statistical-mechanical theory of irreversible processes. I. General theory and simple applications to magnetic and conduction problems. *J. Phys. Soc. Jpn.* **1957**, *12*, 570−586.

(18) Di Ventra, M.; Pershin, Y. V. On the physical properties of memristive, memcapacitive and meminductive systems. *Nanotechnology* **2013**, *24*, No. 255201.

(19) Guo, J.; Lee, J.; Contescu, C. I.; Gallego, N. C.; Pantelides, S. T.; Pennycook, S. J.; Moyer, B. A.; Chisholm, M. F. Crown ethers in graphene. *Nat. Commun.* **2014**, *5*, 5389.

(20) Smolyanitsky, A.; Paulechka, E.; Kroenlein, K. Aqueous Ion Trapping and Transport in Graphene-Embedded 18-Crown-6 Ether Pores. *ACS Nano* **2018**, *12*, 6677−6684.

(21) Fang, A.; Kroenlein, K.; Riccardi, D.; Smolyanitsky, A. Highly mechanosensitive ion channels from graphene-embedded crown ethers. *Nat. Mater.* **2019**, *18*, 76−81.

(22) Kim, H.-m.; Saito, N.; Kim, D.-w. Synthesis of crown-ether-embedded graphene by the solution plasma. *Carbon* **2024**, *216*, No. 118578.

(23) Izatt, R.; Terry, R.; Haymore, B.; Hansen, L.; Dalley, N.; Avondet, A.; Christensen, J. Calorimetric titration study of the interaction of several uni-and bivalent cations with 15-crown-5, 18-crown-6, and two isomers of dicyclohexo-18-crown-6 in aqueous solution at 25. degree. C and. mu.= 0.1. *J. Am. Chem. Soc.* **1976**, *98*, 7620−7626.

(24) Langmuir, I. The Adsorption of Gases on Plane Surfaces of Glass, Mica and Platinum. *J. Am. Chem. Soc.* **1918**, *40*, 1361−1403.

(25) Hall, J. E. Access resistance of a small circular pore. *J. Gen. Physiol.* **1975**, *66*, 531−532.

(26) Stein, D.; Kruithof, M.; Dekker, C. Surface-Charge-Governed Ion Transport in Nanofluidic Channels. *Phys. Rev. Lett.* **2004**, *93*, No. 035901.

(27) Smolyanitsky, A.; Saraniti, M. Silicon nanopores as bioelectronic devices: a simulation study. *J. Comput. Electron.* **2009**, *8*, 90−97.

(28) Joshi, P.; Smolyanitsky, A.; Petrossian, L.; Goryll, M.; Saraniti, M.; Thornton, T. J. Field effect modulation of ionic conductance of cylindrical silicon-on-insulator nanopore array. *J. Appl. Phys.* **2010**, *107*, No. 054701.

(29) Liu, K.; Lihter, M.; Sarathy, A.; Caneva, S.; Qiu, H.; Deiana, D.; Tileli, V.; Alexander, D. T. L.; Hofmann, S.; Dumcenco, D.; et al. Geometrical Effect in 2D Nanopores. *Nano Lett.* **2017**, *17*, 4223−4230.

(30) Jorgensen, W. L.; Maxwell, D. S.; Tirado-Rives, J. Development and Testing of the OPLS All-Atom Force Field on Conformational Energetics and Properties of Organic Liquids. *J. Am. Chem. Soc.* **1996**, *118*, 11225−11236.

(31) Jorgensen, W. L.; Chandrasekhar, J.; Madura, J. D.; Impey, R. W.; Klein, M. L. Comparison of simple potential functions for simulating liquid water. *J. Chem. Phys.* **1983**, *79*, 926−935.

(32) Govind Rajan, A.; Strano, M. S.; Blankschtein, D. Ab Initio Molecular Dynamics and Lattice Dynamics-Based Force Field for Modeling Hexagonal Boron Nitride in Mechanical and Interfacial Applications. *J. Phys. Chem. Lett.* **2018**, *9*, 1584−1591.

(33) Fang, A.; Kroenlein, K.; Smolyanitsky, A. Mechanosensitive Ion Permeation across Subnanoporous MoS_2 Monolayers. *J. Phys. Chem. C* **2019**, *123*, 3588−3593.

(34) Hub, J. S.; de Groot, B. L.; van der Spoel, D. g_wham—A Free Weighted Histogram Analysis Implementation Including Robust Error and Autocorrelation Estimates. *J. Chem. Theory Comput.* **2010**, *6*, 3713−3720.